Research Square

Preprints are preliminary reports that have not undergone peer review.
They should not be considered conclusive, used to inform clinical practice,
or referenced by the media as validated information.

CRISPR/Cas9-mediated miR-155 knockout suppresses glioblastoma cell proliferation through TP53INP1/p53/p21 activation

Jung Bae Seong
Korea Research Institute of Bioscience and Biotechnology
Se-Hee Choe
Korea Research Institute of Bioscience and Biotechnology
Wi-Jae Lee
Chung-Ang University
Sang-Je Park
Korea Research Institute of Bioscience and Biotechnology
Junghyung Park
Korea Research Institute of Bioscience and Biotechnology
Hyoung-Chin Kim
Seoul National University
Jae-Won Huh
Korea Research Institute of Bioscience and Biotechnology
Seung Hwan Lee
Chung-Ang University
Yeongjeon Lee
neurosci@kribb.re.kr

Korea Research Institute of Bioscience and Biotechnology

Article

Keywords: Glioblastoma, microRNA, CRISPR/Cas9, TP53INP1, Cell proliferation

Posted Date: July 22nd, 2026

DOI: https://doi.org/10.21203/rs.3.rs-10352072/v1

License: This work is licensed under a Creative Commons Attribution 4.0 International License.
Read Full License

Additional Declarations: No competing interests reported.

Abstract

MicroRNA-155 (miR-155) has been implicated in glioblastoma (GBM) progression. However, its role remains unclear because previous studies have largely relied on transient modulation approaches and have reported context-dependent effects. Here, we generated stable miR-155 knockout (K/O) U87 and T98G GBM cell lines using CRISPR/Cas9 and examined the effects of sustained miR-155 loss on proliferative and malignancy-associated phenotypes. miR-155 K/O reduced cell viability and clonogenic growth in both cell lines. Ki-67 expression decreased, whereas p21 expression increased in miR-155-deficient cells. Western blot analysis showed increased TP53INP1, p53, and p21 levels, accompanied by Bax induction and Bcl-2 reduction. Confocal imaging demonstrated enhanced nuclear localization of TP53INP1. In contrast, the effects of miR-155 depletion on malignancy-associated markers were heterogeneous between U87 and T98G cells, with TWIST showing the most consistent decrease among the examined markers. Migration was modestly reduced in both cell lines, whereas anti-invasive effects were limited and not consistently observed, particularly in T98G cells. These findings indicate that stable miR-155 deletion suppresses GBM cell proliferation through TP53INP1/p53/p21 activation, while exerting limited effects on other malignancy-related traits.

INTRODUCTION

Glioblastoma (GBM) is the most aggressive primary malignant brain tumor in adults and is associated with a dismal prognosis despite multimodal treatment consisting of maximal safe resection, followed by radiotherapy and temozolomide chemotherapy [1–3]. The median overall survival remains approximately 12–15 months, and long-term survival is rare, with population-based datasets indicating a 5-year survival rate of only 5–7% [1,2]. Nearly all patients eventually experience tumor recurrence, underscoring the profound therapeutic resistance of this disease [2,3]. These clinical limitations highlight the critical need to define the regulatory networks that sustain GBM progression and promote treatment resistence.

Major obstacles to effective therapy are the marked intratumoral heterogeneity and cellular plasticity of GBM. Rather than existing as fixed molecular entities, GBM cells dynamically transition among multiple transcriptional states in response to the genetic background, microenvironmental cues, and therapeutic pressure [4–7]. Single-cell studies have shown that GBMs contain interconvertible malignant cell states resembling developmental neural programs, whereas recurrent tumors frequently undergo therapy-associated state reconfiguration, including the enrichment of mesenchymal-like phenotypes [5–7]. This adaptive flexibility enables tumor cells to rewire the pathways governing proliferation, invasion, stress responses, and survival, thereby contributing to recurrence and treatment resistance.

MicroRNAs (miRNAs) are important post-transcriptional regulators that coordinate complex gene networks involved in tumor initiation, progression, and therapeutic response. Widespread dysregulation of miRNA expression has been documented in GBM, and multiple miRNAs have been implicated in the control of proliferation, apoptosis, stemness, invasion, and chemoradioresistance [8–11]. Because a single miRNA can simultaneously regulate numerous target transcripts, miRNAs function not only as gene

repressors but also as network-level modulators capable of reshaping tumor phenotypes under intrinsic or treatment-induced stress [8–10].

Among these, microRNA-155 (miR-155) is widely recognized as an oncogenic miRNA in diverse malignancies and has been implicated in glioma/GBM biology [10,12]. Previous studies have reported that miR-155 promotes glioma cell proliferation, invasion, and survival by repressing tumor-suppressive pathways involving FOXO3a, MXI1, and stress-associated MAPK signaling [12–15]. In contrast, other studies have suggested that miR-155 exerts context-dependent tumor-suppressive effects in GBM by inhibiting AGTR1-associated oncogenic signaling [16]. These conflicting observations suggest that the biological role of miR-155 in GBM depends on the cellular context, regulatory state, and experimental strategy. Additionally, mature miR-155 produces both the 5p and 3p strands, which may exert distinct or partially overlapping biological effects through different target repertoires [17]. This complexity is further supported by transcriptome-wide analyses showing that miR-155 can regulate gene expression through both canonical and non-canonical target interactions, suggesting that its regulatory range may extend beyond conventional computational predictions [18]. Moreover, miR-155-mediated targeting and expression can vary substantially depending on the cellular context and activation state [19]. These findings support the need for transcriptome-level analyses to understand the functional consequences of sustained miR-155 loss in GBM.

Importantly, most prior studies examining miR-155 in GBM have relied on transient inhibition or overexpression approaches and have primarily focused on limited phenotypic outputs, such as proliferation or migration [12–16]. Such approaches provide only partial insight into how sustained miR-155 loss reshapes interconnected tumor-regulatory networks. This issue may be particularly relevant in GBM, where perturbation of a single regulatory node is likely to produce broader adaptive effects beyond a single linear pathway. Notably, TP53INP1 is a stress-responsive tumor suppressor that enhances p53-dependent transcriptional activity and has been reported to be a downstream target suppressed by miR-155 in other cancer contexts [20,21]. These observations suggested that stable miR-155 depletion may relieve the repression of TP53INP1-associated growth-inhibitory programs in GBM.

Recent advances in CRISPR/Cas9 genome editing have enabled the stable and permanent disruption of miRNA loci, providing a useful framework for dissecting miRNA functions beyond transient modulation models [22]. Supporting this approach, the CRISPR-mediated knockout of miR-21 in glioma models has demonstrated that genomic ablation of an oncogenic miRNA can produce measurable anti-tumor phenotypes [23]. In the present study, we generated stable miR-155 K/O GBM cell lines using CRISPR/Cas9 and examined how sustained miR-155 loss affects the proliferative capacity and malignancy-associated traits. Through integrated molecular and functional, analyses, we showed that miR-155 deletion suppresses GBM cell proliferation in association with TP53INP1/p53/p21 activation, while exerting limited and heterogeneous effects on other malignancy-related phenotypes.

RESULTS

Generation of miR-155 knockout cell lines in human-derived U87 and T98G cells

To investigate the role of miR-155 in GBM cell proliferation, miR-155 knockout (K/O) cell lines were established using human-derived U87 and T98G cells (Fig. 1a). Briefly, a CRISPR/Cas9 expression vector was transfected into GBM cells and GFP-positive cells were isolated. Single-cell clones were subsequently obtained and subjected to sequencing-based validation to selectively identify clones harboring precise knockout of the miR-155 locus. To achieve complete suppression of miR-155 expression in human cells, a dual-targeting strategy was employed using CRISPR/Cas9 directed against both the promoter region and the miR-155 gene body. Guide RNAs were designed to minimize sequence homology to potential off-target sites while enabling precise deletion of the intervening genomic region (Fig. 1b, Supplemental Tables S1 and S2). To optimize targeting efficiency, multiple combinations of CRISPR/Cas9 target sites within the promoter and gene body regions were tested in both U87 and T98G cells. Among these, the simultaneous targeting of sites 2 and 4 resulted in a highly efficient and precise deletion spanning the promoter–miR-155 gene body region (Fig. 1c–f). Based on these results, single-cell clones were isolated from both U87 and T98G cells following CRISPR/Cas9 targeting of the promoter and gene body regions (Fig. 1g, h). Genomic validation identified clones exhibiting precise deletion of the target locus, designated U87-4 and T98G-4 (Fig. 1i). These clones were further expanded in culture and the stability of the deletion was confirmed over subsequent passages (Fig. 1i). To assess the specificity of genome editing, in silico-based targeted amplicon sequencing was performed (Fig. 1j and k). Potential off-target sites were predicted by allowing up to three mismatches relative to the gRNA sequence. This analysis identified two candidate sites for target 2 and ten candidate sites for target 4 in each cell line. Subsequent experimental validation revealed no detectable off-target editing events in either U87-4 (Fig. 1j) or T98G-4 clones (Fig. 1k).

Identification of DEGs in miR-155 knockout cell lines

To systematically investigate the effects of sustained loss of miR-155 on the transcriptome of GBM cells, RNA sequencing was performed on the WT, miR-155 K/O T98G, and U87 cell lines (Fig. 2a). For the selection of differentially expressed genes (DEGs), the criteria $|\log_2 FC| \geq 1$ (2.0-fold change) and adjusted $P < 0.05$ were applied, and the entire list of DEGs is described in Supplementary Table S3 and S4. Volcano plot analysis revealed widespread transcriptomic changes in both miR-155 K/O cell lines. A total of 2,900 genes in the T98G cell line showed significant differences in expression (Fig. 2b), of which 1,335 were upregulated and 1,565 were downregulated. In U87 cells, a total of 2,775 DEGs were identified, of which 1,590 were upregulated and 1,185 were downregulated (Fig. 2b). These results suggest that miR-155 deficiency induces extensive transcriptomic changes in both GBM cell lines.

PCA confirmed that U87 and T98G cells formed distinct transcriptomic clusters consistent with their different cellular backgrounds. Despite these underlying differences between the models, we aimed to identify the key factors commonly regulated by miR-155 K/O through quadrant analysis using the DEG analysis results. A complete list of genes classified in each quadrant is provided in Supplementary Table

S5. The transcriptome changes were visualized by plotting the $\log_2$ FC (LFC) values of the genes from DEG analyses 1 and 2 (Fig. 2c). This analysis revealed that a significant number of genes exhibited consistent expression patterns following miR-155 K/O treatment in both cell lines. Specifically, 138 genes were identified in quadrant 1 (q1: genes upregulated in both cell lines), representing genes that were significantly upregulated in both T98G and U87 cells. Complete enrichment results are provided in Supplementary Table S6. Conversely, 169 genes were identified in quadrant 3 (q3: genes downregulated in both cell lines), representing genes that were consistently downregulated in both models. Quadrants 2 and 4, representing genes with contrasting expression patterns in the two cell lines, contained 147 and 46 genes, respectively. Because miRNAs generally repress target transcripts, genes commonly upregulated after miR-155 K/O are considered useful starting points for identifying candidate miR-155-regulated genes. Therefore, we focused on the quadrant 1 gene set for subsequent target prioritization analysis. This quadrant-based comparison allowed us to define the shared and cell line-specific transcriptomic responses to miR-155 K/O.

Functional characterization of cell-line-specific transcriptomic changes after miR-155 knockout

To characterize the functional consequences of miR-155 K/O in each GBM cell line, we performed gene ontology (GO) and pathway enrichment analyses using the upregulated and downregulated DEG sets from each cell line, while separately highlighting the terms shared between U87 and T98G cells. GO analysis revealed that 591 genes in T98G cells and 851 genes in U87 cells were involved in biological processes (Fig. 3a). Among these, “connective tissue development,” “cell-substrate adhesion,” “axon guidance,” “neuron projection guidance,” and “locomotory behavior” were significantly enriched in both cell lines. Although these common GO terms were consistently enriched in both the cell lines, their statistical significance differed. For example, certain terms such as “connective tissue development” and “cell-substrate adhesion” showed high significance in T98G cells, whereas they were less significantly enriched in U87 cells. To examine the unique biological processes in each cell line in greater detail, we analyzed the enrichment of GO terms specific to each cell line. Excluding the shared biological processes (BP) described above, the T98G cell-specific analysis showed significant enrichment of the terms “cell-matrix adhesion” and “cartilage development”. In U87 cells, "axonogenesis" and "regulation of neuron projection development" were specifically enriched. KEGG pathway analysis revealed that 286 genes in T98G cells and 423 genes in U87 cells mapped to enriched pathways (Fig. 3b). Although there were no KEGG pathways common to both cell lines, "integrin signaling" was the most significantly enriched pathway in T98G cells, whereas "axon guidance" was the most significantly enriched pathway in U87 cells, consistent the functional categories identified in the GO analysis results. Together, these enrichment patterns suggest that miR-155 K/O induces distinct functional transcriptomic responses in the two GBM cell lines, with T98G cells showing stronger extracellular matrix- and adhesion-associated enrichment, and U87 cells showing stronger neural development- and axon guidance-associated enrichment. Next, to better understand the transcriptomic programs that were reduced after miR-155 K/O treatment, we analyzed the downregulated DEG sets from each cell line. GO analysis revealed that

904 genes in T98G cells and 828 genes in U87 cells were associated with enriched biological processes, respectively (Fig. 3c). Commonly downregulated DEGs showed modest enrichment for terms related to “tissue homeostasis” and “anatomical structure homeostasis” across both cell lines. In T98G cells, although most terms showed low statistical significance, “regulation of body fluid level” showed marginal enrichment, suggesting a cell line-specific response. In contrast, several statistically significant enrichments were observed for U87 cells. Terms such as “nucleosome assembly,” “nucleosome organization,” “protein-DNA complex organization,” and “protein localization to CENP-A containing chromatin” indicated U87 cell line-specific enrichment. Next, in the KEGG pathway analysis, we confirmed the enrichment results with low statistical significance in T98G cells. The pathways that enriched in both cell lines are as follows; “integrin signaling”, “PI3K-Akt signaling pathway”, “rheumatoid arthritis”. In the U87 cell line-specific pathways, “systemic lupus erythematosus,” “neutrophil extracellular trap formation,” and “alcoholism” were observed. These downregulated enrichment patterns suggest that miR-155 K/O is associated with the attenuation of distinct cell line-dependent transcriptomic programs, including chromatin- and nucleosome-associated processes in U87 cells and selected survival- or signaling-related pathways in T98G cells. Comprehensive GO and KEGG enrichment results are presented in Supplementary Table S6.

Prioritization of candidate miR-155 targets through integration of transcriptome and in silico prediction datasets

To prioritize candidate miR-155 targets among the genes upregulated after miR-155 K/O, we integrated three datasets: (1) genes commonly upregulated in both U87 and T98G miR-155 K/O cells, (2) miR-155-5p and miR-155-3p targets predicted by miRDB, and (3) miR-155-5p targets predicted by TargetScan. Venn diagram-based comparisons identified TP53INP1 as the only gene shared across all three datasets (Fig. 4a, source data). Thus, TP53INP1 emerged as the most strongly supported target of miR-155. GABARAPL1 and CREBRF overlapped between the commonly upregulated DEG set and the miRDB-predicted target set, suggesting that these genes might also be associated with the miR-155-regulated transcriptomic response, although they were not supported by all three prioritization criteria. A complete list of the genes corresponding to each intersection in the Venn diagram is provided in Supplementary Table S7. To evaluate the extent of TP53INP1 upregulation after miR-155 K/O, we extracted TP53INP1 LFC values from the RNA-seq dataset. TP53INP1 expression increased in both cell lines, with a higher LFC in T98G cells than in U87 cells (T98G: 1.53; U87: 1.02; Fig. 4b). These results further support the idea that TP53INP1 is a leading candidate miR-155 target in both GBM cell models. Next, we performed STRING-based protein-protein interaction analysis using the commonly upregulated DEG set to examine whether the prioritized candidates were positioned within a broader interaction network. When a high-confidence interaction threshold was applied, most of the upregulated DEGs appeared as isolated nodes, whereas TP53INP1 showed detectable interaction potential within the sparse network (Fig. 4c). Together with its consistent upregulation and overlap with both the miRDB and TargetScan prediction datasets, this network feature supported the prioritization of TP53INP1 as the leading candidate miR-155-regulated node for subsequent molecular validation.

miR-155 K/O suppresses GBM cell proliferation with TP53INP1/p53/p21 activation

To determine whether miR-155 K/O affects GBM cell proliferation, we first assessed the viability of U87 and T98G cells using the MTT assay. miR-155 K/O significantly reduced cell viability in both cell lines compared to their respective WT controls (Fig. 5a, b). Consistent with this observation, clonogenic assays revealed decreased colony-forming ability of miR-155 K/O cells in both U87 and T98G cells (Fig. 5c, d). To further assess proliferative capacity and cell cycle regulation, Ki-67 and p21 expression levels were analyzed by confocal microscopy. miR-155 K/O decreased Ki-67 expression and increased p21 expression in both cell lines relative to WT controls (Fig. 5e, f). Western blot analysis showed that miR-155 K/O increased Bax expression and decreased Bcl-2 expression in both U87 and T98G cells (Fig. 5g, h). The increase in Bax expression is consistent with a previous report showing that miR-155-5p inhibition increases Bax expression in U87 glioma cells [24], and the concomitant reduction in Bcl-2 in our models further supports the interpretation that miR-155 loss shifts GBM cells away from a strongly pro-survival state. Since TP53INP1 emerged as a candidate target in the transcriptomic analysis, we next examined TP53INP1-associated signaling. TP53INP1, p53, and p21 protein levels were elevated in miR-155 K/O U87 and T98G cells (Fig. 5g, h), consistent with the upregulation of a TP53INP1/p53/p21-associated growth-restrictive program. Moreover, confocal analysis demonstrated enhanced nuclear accumulation of TP53INP1, together with prominent nuclear p53 signaling in miR-155 K/O cells (Fig. 5i, j). Collectively, these data indicate that miR-155 K/O suppresses GBM cell proliferation in association with the upregulation of TP53INP1/p53/p21-associated signaling and a concurrent shift in apoptosis-associated protein expression.

miR-155 K/O exerts limited effects on malignancy-associated characteristics in GBM cells.

To determine whether miR-155 K/O affects malignant phenotypes beyond proliferation, we evaluated malignancy-associated proteins and the migratory and invasive behaviors of U87 and T98G cells. In U87 cells, miR-155 K/O produced only limited changes in the examined markers, with TWIST showing a marked decrease, whereas the expression of CD44, Nanog, Snail, Slug, vimentin, and E-cadherin remained largely unchanged (Fig. 6a). In contrast, T98G cells displayed a broader but non-uniform response: Nanog, Snail, Slug, Twist, vimentin, and E-cadherin were all reduced, whereas CD44 was not significantly altered (Fig. 6b). Since both mesenchymal-associated markers and E-cadherin were decreased in T98G cells, these changes do not fit a simple EMT reversal model and instead suggest cell-line-specific remodeling of malignancy-associated programs. Functionally, miR-155 K/O reduced migration in both cell lines, as shown by the decrease in both migrated cell counts and stained areas (Fig. 6c). However, the anti-invasive effect was cell line-dependent; invasion was significantly reduced in U87 cells, but not in T98G cells (Fig. 6d). Taken together, these data indicate that stable miR-155 loss exerts heterogeneous and relatively limited effects on malignancy-associated characteristics compared to its clear anti-proliferative effect, and that some of the observed reductions in motility-related readouts may partly reflect diminished proliferative output.

DISCUSSION

In this study, we generated stable miR-155 knockout U87 and T98G GBM cell lines through CRISPR/Cas9-mediated deletion of the miR-155 promoter region (Fig. 1). Using this genetic model, we examined the consequences of sustained miR-155 loss at transcriptomic, molecular, and phenotypic levels. We found that miR-155 knockout induced broad but cell-line-specific transcriptomic remodeling while consistently suppressing proliferative capacity in both cell lines. This shared anti-proliferative phenotype was associated with the activation of TP53INP1/p53/p21-linked growth-restrictive signaling. In contrast, changes in malignancy-associated markers and motility-related phenotypes were heterogeneous, suggesting that miR-155 loss affects GBM cell proliferation more robustly than broader malignant behavior.

RNA-seq analysis showed that miR-155 knockout induced extensive changes in gene expression in both U87 and T98G cells (Fig. 2b). However, the functional orientations of these changes differed between the two models. In T98G cells, the upregulated gene sets were preferentially associated with extracellular matrix- and adhesion-related programs, including cell-matrix adhesion, cell-substrate adhesion, connective tissue development, cartilage development, and integrin-associated signaling (Fig. 3a, b). This interpretation was further supported by GSEA, which showed positive enrichment for the regulation of cartilage development in T98G cells (Supplementary Fig. 2A), consistent with the enrichment pattern observed in the DEG-based analysis. Because ECM remodeling and integrin-associated signaling are closely linked to glioma cell adhesion, invasion, and microenvironmental adaptation, this pattern suggests that miR-155 loss induces substantial remodeling of extracellular structural and adhesive programs in T98G cells [25]. In contrast, U87 cells showed preferential enrichment of axon guidance, neuron projection, and axonogenesis-related programs among the upregulated DEGs (Fig. 3a, b). Axon guidance-related molecules and neurodevelopmental programs have been implicated in glioma cell motility and brain infiltration, and the enrichment of these programs in U87 cells is consistent with the reduced invasive phenotype observed in this model [26,27]. However, neuronal lineage conversion was not evaluated in this study. Instead, the U87-specific transcriptomic response may reflect remodeling of neural state-associated, structural plasticity-related, or motility-related regulatory programs. This interpretation is conceptually consistent with previous studies showing that enforced neuronal reprogramming suppresses glioma cell proliferation and tumorigenic potential [28]. Taken together, these cell line-specific transcriptomic signatures suggest that miR-155 loss reshapes distinct cell states and malignancy-associated regulatory programs in each GBM model. The T98G-biased ECM/adhesion-associated transcriptional pattern was accompanied by a broader reduction in malignancy-associated proteins, including Nanog, Snail, Slug, Twist, and vimentin (Fig. 6b). However, because E-cadherin was also reduced and invasion was not consistently suppressed, these changes should be interpreted as partial remodeling of malignancy-associated programs rather than a simple EMT reversal. In U87 cells, axon guidance and neural development-associated enrichment may underlie the reduced invasion phenotype observed in this model. Thus, the divergent transcriptomic signatures were consistent with the heterogeneous malignancy-associated phenotypes observed in U87 and T98G cells.

To identify candidate miR-155-regulated genes that are commonly altered in both GBM cell lines, we focused on convergent gene-level changes rather than global pathway enrichment. Because miRNAs primarily repress target transcripts, genes commonly upregulated after miR-155 knockout may include candidate transcripts released from miR-155-associated repression; however, RNA-seq alone cannot establish direct targeting. By integrating the commonly upregulated DEG set with miRDB and TargetScan prediction datasets, TP53INP1 emerged as the most consistently shared candidate miR-155-regulated gene in both U87 and T98G cells. This finding provided a rationale for subsequent molecular validation, which confirmed increased TP53INP1 protein expression and elevated p53 and p21 levels in both miR-155 knockout cell lines (Fig. 5g, h). Confocal imaging showed enhanced nuclear accumulation of TP53INP1 and p53 in miR-155-deficient cells (Fig. 5i, j). These molecular findings were functionally consistent with reduced cell viability, impaired clonogenic growth, decreased Ki-67 expression, and increased p21 expression in both U87 and T98G cells. Thus, although the global transcriptomic response to miR-155 loss was cell-line-specific, both models converged on a TP53INP1/p53/p21-associated growth-restrictive program.

Additional transcriptomic signatures may further support the reduced proliferative fitness in a cell line-dependent manner. In U87 cells, the downregulated terms related to nucleosome assembly, nucleosome organization, and protein-DNA complex organization may reflect the attenuation of chromatin maintenance programs associated with active cell cycle progression and proliferative demand (Fig. 3c). In T98G cells, downregulation of PI3K-Akt and HIF-1 signaling may indicate a weakening of survival- and stress-adaptive pathways that support GBM cell growth (Fig. 3d) [29,30]. Therefore, the transcriptomic data support the anti-proliferative phenotype at two levels: first, through the identification of TP53INP1 as a shared candidate miR-155-regulated node, and second, through cell-line-specific attenuation of pathways associated with proliferative or survival capacity.

The increase in p21 and reduction in Ki-67 levels suggested that miR-155 knockout restricted cell cycle progression in both U87 and T98G cells. However, the upstream route leading to p21 induction may differ between the two cell lines because U87 and T98G possess distinct genetic backgrounds, including differences in p53 status [31,32]. Thus, miR-155 loss may converge on p21-associated growth inhibition through partially distinct regulatory routes in U87 and T98G cells. In addition to the TP53INP1/p53/p21 axis, miR-155 knockout shifted apoptosis-associated protein expression toward a less pro-survival state, as indicated by Bax induction and Bcl-2 reduction in both U87 and T98G cells (Fig. 5g, h). This pattern is consistent with previous reports showing that miR-155 inhibition promotes apoptosis-related changes in glioma cells [24]. These changes should be interpreted as pro-death priming or increased stress vulnerability, rather than evidence of overt apoptosis. Therefore, the dominant phenotype observed in this study is best described as a reduced proliferative capacity accompanied by growth-restrictive and stress-sensitizing molecular changes.

The heterogeneous effects of miR-155 knockout on malignancy-associated traits were also evident at both the protein and functional levels. In T98G cells, miR-155 knockout broadly reduced several EMT- and stemness-associated proteins, including Nanog, Snail, Slug, Twist, and vimentin, whereas CD44 was not

markedly altered, and E-cadherin was decreased (Fig. 6b). Therefore, these changes do not support a simple EMT-reversal model but rather indicate partial remodeling of malignancy-associated programs. In U87 cells, the changes in EMT- and stemness-associated proteins were limited, with TWIST showing the most consistent decrease. Functionally, migration was significantly but modestly reduced in both cell lines (Fig. 6c), whereas invasion was significantly reduced in U87 cells but not consistently suppressed in T98G cells (Fig. 6d). Because Transwell migration readouts can be influenced by cell number, viability, and proliferative output during the assay period, a modest decrease in migration should be interpreted cautiously and may partly reflect reduced proliferative capacity rather than a direct and robust suppression of migration machinery. Taken together, these findings indicate that miR-155 knockout can partially attenuate malignancy-associated features at the marker level, particularly in T98G cells, but does not uniformly suppress the broader malignant phenotype.

This distinction is important to interpret the biological role of miR-155 in GBM. Previous studies have reported that miR-155 promotes glioma proliferation and invasion through FOXO3a and MXI1-associated mechanisms [12,13], and can regulate proliferative signaling through the PI3K/AKT pathway [33]. Additionally, miR-155 has been implicated in glioma chemosensitivity and temozolomide resistance through MAPK13/MAPK14- and Six1-associated mechanisms [14,34]. Other studies have suggested that miR-155 exerts context-dependent tumor-suppressive effects in specific GBM settings, such as by inhibiting AGTR1-associated oncogenic signaling [16]. These findings are consistent with the context-dependent view. Our stable knockout models are consistent with this non-uniform view, showing a reproducible growth-restrictive response but variable effects on motility- and malignancy-associated traits.

Our findings have several potential therapeutic implications. As temozolomide remains a central component of standard GBM therapy, miR-155-targeted strategies may be more relevant as sensitizing approaches than as standalone interventions. Previous studies have reported that miR-155 inhibition can influence chemosensitivity in glioma-related models, including the response to temozolomide and taxol [14,15,34,35]. In this context, the TP53INP1/p53/p21-associated growth-restrictive response and Bax/Bcl-2 shift observed in our knockout cells suggest that miR-155 depletion may reduce proliferative fitness and increase vulnerability to additional therapeutic stress. However, because miR-155 knockout alone did not uniformly suppress invasion or broader malignancy-associated features, future studies should test whether miR-155 inhibition enhances therapeutic responses in combination settings.

These therapeutic implications should be interpreted with caution owing to several limitations. First, this study used a whole miR-155 knockout rather than strand-specific modulation. Mature miR-155 produces both miR-155-5p and miR-155-3p, which may have distinct or partially overlapping target repertoires [17]. Therefore, the present data do not determine which strand primarily mediates the observed antiproliferative phenotype or cell line-specific transcriptomic responses. Second, although TP53INP1 was identified as a shared candidate miR-155-regulated gene and was validated at the protein level, rescue experiments were not performed. Therefore, the causal role of TP53INP1 in miR-155 knockout-induced growth suppression remains unclear. Third, the present study was performed in tumor-cell-

autonomous in vitro systems and, therefore, did not capture the contribution of the immune microenvironment. This limitation is important because GBM contains abundant tumor-associated macrophages and microglia [36], and miR-155 broadly regulates immune cell functions involved in anti-tumor immunity [37–42]. Therefore, the in vivo consequences of nonselective miR-155 inhibition may differ from those observed in isolated GBM cells. Future studies should evaluate miR-155-targeted strategies in immune-relevant co-cultures or in vivo models.

Collectively, our findings indicate that stable miR-155 knockout suppresses GBM cell proliferation in association with a convergent TP53INP1/p53/p21-associated growth-restrictive program despite the induction of cell-line-specific transcriptomic remodeling in U87 and T98G cells. Transcriptomic data suggested that miR-155 loss remodeled distinct cellular programs in each GBM background, including extracellular matrix (ECM)- and adhesion-associated programs in T98G cells and neural development- and axon guidance-associated programs in U87 cells. However, the most consistent phenotype across both models was a reduced proliferative capacity, whereas changes in malignancy-associated traits were partial and heterogeneous. These results support a model in which miR-155 contributes more robustly to proliferative maintenance than to the uniform control of broader malignant behavior in GBM cells.

METHODS

Cell culture

Human glioblastoma cell lines U87 and T98G were obtained from the American Type Culture Collection (ATCC, VA, USA). Cells were maintained in Dulbecco's modified Eagle's medium (DMEM; Wellgene, Korea) supplemented with 10% fetal bovine serum (FBS; Thermo Fisher Scientific, MA, USA) and 1% penicillin–streptomycin (Wellgene) at 37°C in a humidified incubator with 5% CO2. Cells were routinely passaged at 70–80% confluence.

Generation of stable miR-155 K/O cell lines

Stable miR-155-knockout (miR-155 K/O) U87 and T98G cell lines were established using two CRISPR/Cas9 constructs. The SpCas9-GFP plasmid (pCAG-SpCas9-GFP-U6-gRNA; Addgene #79144) was used as the backbone for sgRNA cloning targeting the miR-155 locus. To enable antibiotic selection, a puromycin-resistant construct (SpCas9-Puro) was generated by replacing the GFP cassette with a puromycin resistance gene via subcloning. Two sgRNA sequences targeting the miR-155 locus (Target 2: 5'-GTTAATGCTAATCGTGATAGGGG-3'; Target 4: 5'-AGCAAGCCTTCAGCACTCAGAGG-3') were individually cloned into each vector. Cells were seeded in 6-well plates at a density of 5×10^4 cells/well and co-transfected with both SpCas9-GFP and SpCas9-Puro constructs using Lipofectamine™ 3000 (Thermo Fisher Scientific, MA, USA) reagent according to the manufacturer's instructions. After transfection, cells were subjected to puromycin selection for 2 weeks using 1.5 μg/mL puromycin for U87 cells and 2

μg/mL puromycin for T98G cells, with the culture medium replaced every 48 h. Following puromycin selection, GFP-positive cells were isolated to enrich for cells carrying both constructs. Single-cell clones were isolated by limiting dilution, and knockout efficiency was confirmed by next-generation sequencing (NGS).

Targeted amplicon sequencing and data analysis

To evaluate potential off-target effects in the generated miR-155 K/O cell lines, candidate off-target sites were first predicted in silico using Cas-OFFinder (http://www.rgenome.net/), a web-based analysis tool, with a mismatch threshold of up to 3 mismatches relative to each sgRNA sequence. For each predicted site, targeted amplicon PCR was performed using site-specific primers (denaturation: 98°C for 30 s, primer annealing: 60°C for 15 s, and elongation: 72°C for 15 s for 35 cycles) to obtain DNA amplicons. For barcoding, nested PCR was subsequently conducted to attach adapter and index sequences to both ends of each amplicon (denaturation: 98°C for 30 s, primer annealing: 62°C for 15 s, and elongation: 72°C for 15 s for 35 cycles). The indexed amplicon mixture was pretreated and loaded into a MiniSeq analyzer (Illumina MiniSeq system, SY-420-1001) according to the manufacturer's protocol to perform targeted amplicon sequencing. The resulting FASTQ files were analyzed using Cas-Analyzer (http://www.rgenome.net/cas-analyzer/), a web-based analysis tool, to calculate the off-target editing efficiency (%) at each predicted site.

Validation of miR-155 K/O by quantitative real-time PCR

Total RNA, including small RNAs, was extracted from WT and miR-155 K/O U87 and T98G cells using the miRNeasy Tissue/Cells Advanced Mini Kit (Qiagen, Hilden, Germany) according to the manufacturer’s instructions. For mature miRNA analysis, reverse transcription was performed using the miRCURY LNA RT Kit (Qiagen). Quantitative real-time PCR was then carried out using the miRCURY LNA Probe PCR Kit (Qiagen) with hsa-miR-155-5p miRCURY LNA miRNA Probe PCR Assay and SNORD48 miRCURY LNA miRNA Probe PCR Assay (Qiagen). SNORD48 was used as the endogenous reference control.

RNA sequencing

Cells were harvested using the lysis reagent of commercial kit, and total RNAs were extracted according to the manufacturer’s protocol (RNAeasy Plus mini kit, Qiagen). The integrity of the extracted RNA was verified using an Agilent Technologies 4200 TapeStation system, and only high-quality RNA samples (RIN > = 7.0) were used for library preparation. mRNA was selectively purified with oligo-dT beads, fragmented, and used as a template for first- and second-strand cDNA synthesis. And then a sequencing library was produced through end-repair and adapter ligation. The generated libraries were sequenced by Macrogen Co., Ltd Illumina Sequencing by Synthesis (SBS) technology, which employs a proprietary reversible terminator based method for high accuracy. The resulting datasets were stored in FASTQ compression format.

RNA-seq data processing

The raw FASTQ reads (Read 1 and 2) were subjected to quality control and adapter trimming using Trim Galore (v0.6.10). The processed reads were aligned to the human reference genome (Homo sapiens GRCh38) using STAR aligner (v2.7.9a). Following alignment, the number of reads mapped to each gene was quantified using HTSeq-count. The resulting count matrix for each sample was then used for downstream differential expression gene (DEG) analysis and functional pathway enrichment analysis to characterize the transcriptomic landscape.

Bioinformatics analysis

Statistical analysis, including PCA and expression data normalization, was performed in the R (version 4.5.2) environment. To visualize variability between samples and evaluate RNA sequencing data quality, the raw count matrix was normalized by applying the Variance Stabilizing Transformation (VST) from the DESeq2 package. Based on the normalized data, Principal Component Analysis (PCA) was conducted to evaluate the similarity between samples according to cell line and experimental condition, and the results were visualized using ggplot2. The PCA plot showed the overall quality of RNA sample, library preparation, and sequencing (supplementary Fig. 1). Differentially expressed genes (DEGs) analysis was performed using DESeq2 to identify changes in miR-155 K/O conditions compared to Wild-type (WT) for each cell line (T98G, U87). Gene expression levels were tested for statistical significance using the Wald test, and Ensembl (release 114) annotation information was merged for accurate gene identification. Differentially expressed genes were defined using a threshold of $|\log2 \text{ fold change}| \geq 1$ and adjusted P-value (Padj) < 0.05.

Functional annotation and pathway analysis

To elucidate the biological functions of the identified DEGs, we performed multi-layered functional enrichment analyses using the clusterProfiler (v4.4.4) and ReactomePA packages. First, we conducted Gene Ontology (GO) analysis on gene sets that were commonly up-regulated or down-regulated in both cell lines to identify enriched terms in the Biological Process (BP) and Molecular Function (MF) categories. Statistical significance was defined as $P_{adj} < 0.1$, corrected via the Benjamini-Hochberg (BH) method. Additionally, biological pathways activated or inhibited by miR-155 K/O were precisely evaluated for each cell line through pathway comparison analysis (compareCluster) based on the Reactome database. To investigate the functional network and connectivity of key DEGs, a Protein-Protein Interaction (PPI) network analysis was conducted using the STRING (https://string-db.org) web-based tools. Furthermore, to provide a comprehensive functional analysis that does not rely on specific cutoff values of the gene list, Gene Set Enrichment Analysis (GSEA) was performed on the entire transcriptome. All genes were ranked in descending order based on their $\log_2$ Fold Change (LFC) values, and the Normalized Enrichment Score (NES) for the GO BP database was calculated using the gseGO function. The analysis results were visualized by classifying them into Activated (NES > 0) and Suppressed (NES < 0) pathways, and all visualization processes were configured using dotplot and ggplot2 to enable intuitive interpretation of the data.

Prioritization and statistical filtering of miR-155 targets

We utilized two independent bioinformatics prediction algorithms: miRDB (v6.0) [43] and TargetScan (Human v8.0) [44]. Predicted targets were retrieved from miRDB (https://mirdb.org/) for miR-155 as a keyword and downloaded two predicted target files, miR-155-5p and miR-155-3p. To ensure high prediction reliability, we retained only targets with a miRDB Target Score of 80 or higher. Using this criterion, 238 of the 701 predicted targets for miR-155-5p and 97 of the 422 predicted targets for miR-155-3p were selected. After removing duplicate genes, we conducted a follow-up analysis on a total of 332 unique genes in miRDB. Second, for TargetScan, we focused specifically on the miR-155-5p strand. This decision was in accordance with the database's technical guidelines, which reflect warnings that − 3p strand predictions have lower reliability, higher false positive rates, and may be less likely to be functional targets compared to the − 5p strand. We searched the TargetScan web page (https://www.targetscan.org/vert_80/) using the keyword 'miR-155' to obtain files of the 556 initial predicted targets of miR-155-5p. Among these, we filtered out genes with a cumulative weighted context + + score of less than − 0.4. By applying this strict criterion, we selected 46 highly confident targets. Finally, target genes obtained from the two databases were integrated with the transcriptomic dataset and used to select key regulatory factors.

Cell proliferation assay

Cell proliferation was assessed using the MTT assay. Briefly, WT and miR-155 K/O U87 and T98G cells were seeded in 96-well plates at a density of 2 × 10^3 cells per well. Cell viability was measured daily for 6 days using MTT reagent (1 mg/mL; Thermo Fisher Scientific) prepared in phenol red-free MEM (Wellgene), with 50 µL added to each well. After incubation with MTT solution for 2 h, the generated formazan crystals were dissolved in isopropanol, and absorbance was measured at 570 nm using a microplate reader (Eon; BioTek Instruments, VT, USA). Results were expressed as a percentage relative to the WT group.

Clonogenic assay

For colony formation assays, U87 cells were seeded at 4 × 10^3 cells per well and T98G cells were seeded at 3 × 10^3 cells per well in 6-well plate. Cells were cultured for 9 days under standard growth conditions, with medium changed every 3 days. At the end of the incubation period, colonies were fixed with MeOH and stained with crystal violet (Thermo Fisher Scientific).

Immunofluorescence staining

For immunofluorescence analysis, WT and miR-155 K/O cells were seeded onto glass coverslips and allowed to attach overnight. Cells were fixed with 4% paraformaldehyde for 2 h, permeabilized with 0.25% Triton X-100 in PBS for 20 min, and blocked with 1% BSA, 0.25% Triton X-100 in PBS for 1 h at room temperature. Cells were then incubated overnight at 4°C with primary antibodies against Ki-67 (#9949; Cell signaling, MA, USA), p21 (#2947), p53 (#2524), or TP53INP1 (ab202026; Abcam, MA, USA). After washing, cells were incubated with species-appropriate fluorescent secondary antibodies (Thermo Fisher Scientific, 1000:1) overnight at 4°C in the dark. Nuclei were counterstained with DAPI-containing medium (VECTASHIELD, CA, USA). Fluorescence images were acquired using a confocal laser scanning

microscope (LSM-710; Carl Zeiss, Jena, Germany). For proliferative and cell cycle analyses, Ki-67 and p21 fluorescence signals were compared between WT and miR-155 K/O cells. TP53INP1 subcellular localization was evaluated by confocal microscopy based on its nuclear distribution relative to DAPI staining.

Western blot analysis

Cells were lysed in PRO-PREP protein extraction solution containing protease and phosphatase inhibitors (iNtRON, Republic of Korea). Protein concentration was determined using a NanoDrop spectrophotometer (Thermo Fisher Scientific). Equal amounts of protein were separated by SDS-PAGE and transferred onto PVDF membranes (Thermo Fisher Scientific). Membranes were blocked with 5% BSA in TBS-T for 1 h and incubated overnight at 4°C with primary antibodies against TP53INP1 (ab202026; Abcam, MA, USA), p53 (#2524; Cell signaling, MA, USA), p21 (#2947), Bcl-2 (#3498), Bax (#14796), CD44 (#3570), Slug (#9585), Snail (#3879), Twist (#69366), vimentin (#5741), E-cadherin (#3195), GAPDH (#2118) and Nanog (AF;1997, Novus Biologicals, CO, USA). After incubation with horseradish peroxidase-conjugated secondary antibodies (Cell signaling, 5000:1), immunoreactive bands were visualized using an enhanced chemiluminescence detection system and imaged using ChemiDoc (Bio-Rad Laboratories, CA, USA). Band intensities were quantified using ImageJ software and normalized to GAPDH.

Cell migration assay

Cell migration was assessed using Transwell inserts with 8-μm pore membranes (SPL Life Sciences, Republic of Korea) in 24-well plates. The upper surface of the membrane was coated with collagen I (Advanced BioMatrix, CA, USA) at a final concentration of 50 ng/mL. WT and miR-155 K/O cells were suspended in serum-free medium, and 5 × 10^4 cells were seeded into the upper chamber. Medium containing 10% FBS was added to the lower chamber as a chemoattractant. After 24 h incubation, non-migrated cells on the upper surface of the membrane were removed with a cotton swab. Cells that had migrated to the lower surface were fixed with MeOH and stained with crystal violet (Sigma). Images were acquired under a light microscope, and migrated cells were quantified by cell counting per field and/or stained area measurement using ImageJ software.

Cell invasion assay

Cell invasion assays were performed using 24-well Transwell inserts with 8-μm pore membranes precoated with Matrigel (Corning, NY, USA) diluted 1:10 in serum-free medium. WT and miR-155 K/O cells (1 × 10^5 cells per insert) were seeded into the upper chamber in serum-free medium, while complete medium was added to the lower chamber. After 24 h incubation, non-invaded cells and residual Matrigel on the upper surface of the membrane were gently removed. Invaded cells on the lower surface were fixed, stained with crystal violet, and analyzed under a light microscope. Invasion was quantified by counting invaded cells per field and/or measuring stained area using ImageJ software.

Statistical analysis

All quantitative data are presented as mean ± SEM. Unless otherwise indicated, all experiments were performed in at least three independent biological replicates. RNA-seq analysis was performed using three biological replicates per group. Western blotting, immunofluorescence, clonogenic, migration, and invasion assays were repeated at least three times independently. MTT assays were performed with six technical replicate wells per condition and repeated in independent experiments. Statistical analyses were performed using GraphPad Prism version 11 (GraphPad Software, San Diego, CA, USA). For quantitative comparisons in Fig. 1, multiple unpaired t-tests with Holm–Šídák correction were used where multiple comparisons were performed. For MTT cell viability assays, two-way ANOVA followed by Šídák's multiple comparisons test was used. For other two-group comparisons, two-tailed Welch's t-test was used. $P < 0.05$ was considered statistically significant. Statistical significance was defined as ns, not significant; *$P < 0.05$, **$P < 0.01$, ***$P < 0.001$, and ****$P < 0.0001$.

Declarations

Competing interests

The authors declare no competing interests.

Funding

This research was supported by the Korea Research Institute of Bioscience and Biotechnology (KRIBB) Research Initiative Program (KGM4562633), the Korea Health Technology R&D Project through the Korea Health Industry Development Institute (KHIDI), funded by the Ministry of Health & Welfare, Republic of Korea (RS-2024-00439579), and the National Research Foundation funded by the Korean Ministry of Education, Science, and Technology (RS-2025-00554011).

Author Contribution

ContributionsJ.B.S., S.H.L., and Y.L. conceived and designed the study. J.B.S., S.H.C., W.J.L., S.J.P., and J.P. performed the experiments and analyzed the data. J.B.S., S.H.C., H.C.K., and W.J.L. contributed to figure preparation and data interpretation. J.W.H., S.H.L., and Y.L. supervised the study. J.B.S., S.H.C., and W.J.L. wrote the manuscript. All authors reviewed and approved the final manuscript.

Data Availability

All data generated or analyzed during this study are included in this article and its Supplementary Information files. Additional data supporting the findings of this study are available from the corresponding author upon reasonable request.

References

1. Miller, K. D. et al. Brain and other central nervous system tumor statistics, 2021. *CA Cancer J. Clin.* **71**, 381–406. 10.3322/caac.21693 (2021).
2. Stupp, R. et al. Radiotherapy plus concomitant and adjuvant temozolomide for glioblastoma. *N Engl. J. Med.* **352**, 987–996. 10.1056/NEJMoa043330 (2005).
3. Lim, M., Xia, Y., Bettegowda, C. & Weller, M. Current state of immunotherapy for glioblastoma. *Nat. Rev. Clin. Oncol.* **15**, 422–442. 10.1038/s41571-018-0003-5 (2018).
4. Verhaak, R. G. et al. Integrated genomic analysis identifies clinically relevant subtypes of glioblastoma characterized by abnormalities in PDGFRA, IDH1, EGFR, and NF1. *Cancer Cell.* **17**, 98–110. 10.1016/j.ccr.2009.12.020 (2010).
5. Neftel, C. et al. An Integrative Model of Cellular States, Plasticity, and Genetics for Glioblastoma. *Cell* 178, 835–849 e821, (2019). 10.1016/j.cell.2019.06.024
6. Couturier, C. P. et al. Single-cell RNA-seq reveals that glioblastoma recapitulates a normal neurodevelopmental hierarchy. *Nat. Commun.* **11**, 3406. 10.1038/s41467-020-17186-5 (2020).
7. Wang, L. et al. A single-cell atlas of glioblastoma evolution under therapy reveals cell-intrinsic and cell-extrinsic therapeutic targets. *Nat. Cancer*. **3**, 1534–1552. 10.1038/s43018-022-00475-x (2022).
8. Banelli, B. et al. MicroRNA in Glioblastoma: An Overview. *Int J Genomics* 7639084, (2017). 10.1155/2017/7639084 (2017).
9. Rezaei, O., Honarmand, K., Nateghinia, S., Taheri, M. & Ghafouri-Fard miRNA signature in glioblastoma: Potential biomarkers and therapeutic targets. *Exp. Mol. Pathol.* **117**, 104550. 10.1016/j.yexmp.2020.104550 (2020).
10. Ordonez-Rubiano, E. G. et al. The potential of miRNA-based approaches in glioblastoma: An update in current advances and future perspectives. *Curr. Res. Pharmacol. Drug Discov*. **7**, 100193. 10.1016/j.crphar.2024.100193 (2024).
11. Ciafre, S. A. et al. Extensive modulation of a set of microRNAs in primary glioblastoma. *Biochem. Biophys. Res. Commun.* **334**, 1351–1358. 10.1016/j.bbrc.2005.07.030 (2005).
12. Ling, N. et al. microRNA-155 regulates cell proliferation and invasion by targeting FOXO3a in glioma. *Oncol. Rep.* **30**, 2111–2118. 10.3892/or.2013.2685 (2013).
13. Zhou, J. et al. MicroRNA-155 promotes glioma cell proliferation via the regulation of MXI1. *PLoS One*. **8**, e83055. 10.1371/journal.pone.0083055 (2013).
14. Liu, Q. et al. miR-155 Regulates Glioma Cells Invasion and Chemosensitivity by p38 Isforms In Vitro. *J. Cell. Biochem.* **116**, 1213–1221. 10.1002/jcb.25073 (2015).
15. Meng, W. et al. Anti-miR-155 oligonucleotide enhances chemosensitivity of U251 cell to taxol by inducing apoptosis. *Cell. Biol. Int.* **36**, 653–659. 10.1042/CBI20100918 (2012).
16. Singh, A., Srivastava, N., Yadav, A., Ateeq, B. & Targeting AGTR1/NF-kappaB/CXCR4 axis by miR-155 attenuates oncogenesis in glioblastoma. *Neoplasia* **22**, 497–510. 10.1016/j.neo.2020.08.002 (2020).

17. Mitra, R., Adams, C. M., Jiang, W., Greenawalt, E. & Eischen, C. M. Pan-cancer analysis reveals cooperativity of both strands of microRNA that regulate tumorigenesis and patient survival. *Nat. Commun.* **11**, 968. 10.1038/s41467-020-14713-2 (2020).
18. Loeb, G. B. et al. Transcriptome-wide miR-155 binding map reveals widespread noncanonical microRNA targeting. *Mol. Cell.* **48**, 760–770. 10.1016/j.molcel.2012.10.002 (2012).
19. Hsin, J. P., Lu, Y., Loeb, G. B., Leslie, C. S. & Rudensky, A. Y. The effect of cellular context on miR-155-mediated gene regulation in four major immune cell types. *Nat. Immunol.* **19**, 1137–1145. 10.1038/s41590-018-0208-x (2018).
20. Shahbazi, J., Lock, R. & Liu, T. Tumor Protein 53-Induced Nuclear Protein 1 Enhances p53 Function and Represses Tumorigenesis. *Front. Genet.* **4**, 80. 10.3389/fgene.2013.00080 (2013).
21. Gironella, M. et al. Tumor protein 53-induced nuclear protein 1 expression is repressed by miR-155, and its restoration inhibits pancreatic tumor development. *Proc. Natl. Acad. Sci. U S A*. **104**, 16170–16175. 10.1073/pnas.0703942104 (2007).
22. Chang, H. et al. CRISPR/cas9, a novel genomic tool to knock down microRNA in vitro and in vivo. *Sci. Rep.* **6**, 22312. 10.1038/srep22312 (2016).
23. Nieland, L. et al. CRISPR-Cas knockout of miR21 reduces glioma growth. *Mol. Ther. Oncolytics*. **25**, 121–136. 10.1016/j.omto.2022.04.001 (2022).
24. Guo, Z. et al. MiR-155-5p regulates autophagy and apoptosis of glioma cells through RICTOR. *Transl Cancer Res.* **13**, 5509–5521. 10.21037/tcr-24-543 (2024).
25. Ellert-Miklaszewska, A., Poleszak, K., Pasierbinska, M. & Kaminska, B. Integrin Signaling in Glioma Pathogenesis: From Biology to Therapy. *Int. J. Mol. Sci.* **21** 10.3390/ijms21030888 (2020).
26. Mair, D. B., Ames, H. M. & Li, R. Mechanisms of invasion and motility of high-grade gliomas in the brain. *Mol. Biol. Cell.* **29**, 2509–2515. 10.1091/mbc.E18-02-0123 (2018).
27. Seker-Polat, F., Pinarbasi Degirmenci, N., Solaroglu, I. & Bagci-Onder, T. Tumor Cell Infiltration into the Brain in Glioblastoma: From Mechanisms to Clinical Perspectives. *Cancers (Basel)*. 14. 10.3390/cancers14020443 (2022).
28. Cheng, X. et al. Inhibition of Glioma Development by ASCL1-Mediated Direct Neuronal Reprogramming. *Cells* **8** 10.3390/cells8060571 (2019).
29. Hashemi, M. et al. Progress in targeting PTEN/PI3K/Akt axis in glioblastoma therapy: Revisiting molecular interactions. *Biomed. Pharmacother*. **158**, 114204. 10.1016/j.biopha.2022.114204 (2023).
30. Domenech, M., Hernandez, A., Plaja, A., Martinez-Balibrea, E. & Balana, C. Hypoxia: The Cornerstone of Glioblastoma. *Int J Mol Sci* 22, (2021). 10.3390/ijms222212608
31. Godoy, P. R. et al. Ionizing radiation-induced gene expression changes in TP53 proficient and deficient glioblastoma cell lines. *Mutat. Res.* **756**, 46–55. 10.1016/j.mrgentox.2013.06.010 (2013).
32. Ramao, A. et al. Changes in the expression of proteins associated with aerobic glycolysis and cell migration are involved in tumorigenic ability of two glioma cell lines. *Proteome Sci.* **10**, 53. 10.1186/1477-5956-10-53 (2012).

33. Wu, D. & Wang, C. miR-155 Regulates the Proliferation of Glioma Cells Through PI3K/AKT Signaling. *Front. Neurol.* **11**, 297. 10.3389/fneur.2020.00297 (2020).
34. Chen, G., Chen, Z. & Zhao, H. MicroRNA-155-3p promotes glioma progression and temozolomide resistance by targeting Six1. *J. Cell. Mol. Med.* **24**, 5363–5374. 10.1111/jcmm.15192 (2020).
35. Ozpak, L., Goker Bagca, B., Biray Avci, C., Gunduz, C. & Durmaz, B. Anti-miRNA- 155–5p enhances the cytotoxic efficacy of temozolomide in brain cancer stem cells. *Naunyn Schmiedebergs Arch. Pharmacol.* **398**, 12757–12772. 10.1007/s00210-025-04135-6 (2025).
36. Khan, F. et al. Macrophages and microglia in glioblastoma: heterogeneity, plasticity, and therapy. *J. Clin. Invest.* **133** 10.1172/JCI163446 (2023).
37. Li, P. et al. MicroRNA-155 Promotes Heat Stress-Induced Inflammation via Targeting Liver X Receptor alpha in Microglia. *Front. Cell. Neurosci.* **13** 10.3389/fncel.2019.00012 (2019).
38. Monnot, G. C. et al. miR-155 Overexpression in OT-1 CD8(+) T Cells Improves Anti-Tumor Activity against Low-Affinity Tumor Antigen. *Mol. Ther. Oncolytics*. **16**, 111–123. 10.1016/j.omto.2019.12.008 (2020).
39. Dudda, J. C. et al. MicroRNA-155 is required for effector CD8 + T cell responses to virus infection and cancer. *Immunity* **38**, 742–753. 10.1016/j.immuni.2012.12.006 (2013).
40. Wang, J. et al. MicroRNA-155 deficiency enhances the recruitment and functions of myeloid-derived suppressor cells in tumor microenvironment and promotes solid tumor growth. *Int. J. Cancer*. **136**, E602–613. 10.1002/ijc.29151 (2015).
41. Chen, S. et al. Host miR155 promotes tumor growth through a myeloid-derived suppressor cell-dependent mechanism. *Cancer Res.* **75**, 519–531. 10.1158/0008-5472.CAN-14-2331 (2015).
42. Kalkusova, K., Taborska, P., Stakheev, D. & Smrz, D. The Role of miR-155 in Antitumor Immunity. *Cancers (Basel)*. **14** 10.3390/cancers14215414 (2022).
43. Chen, Y. H. & Wang, X. W. miRDB: an online database for prediction of functional microRNA targets. *Nucleic Acids Res.* **48**, D127–D131. 10.1093/nar/gkz757 (2020).
44. McGeary, S. E. et al. The biochemical basis of microRNA targeting efficacy. *Science* **366** 10.1126/science.aav1741 (2019).

Figures

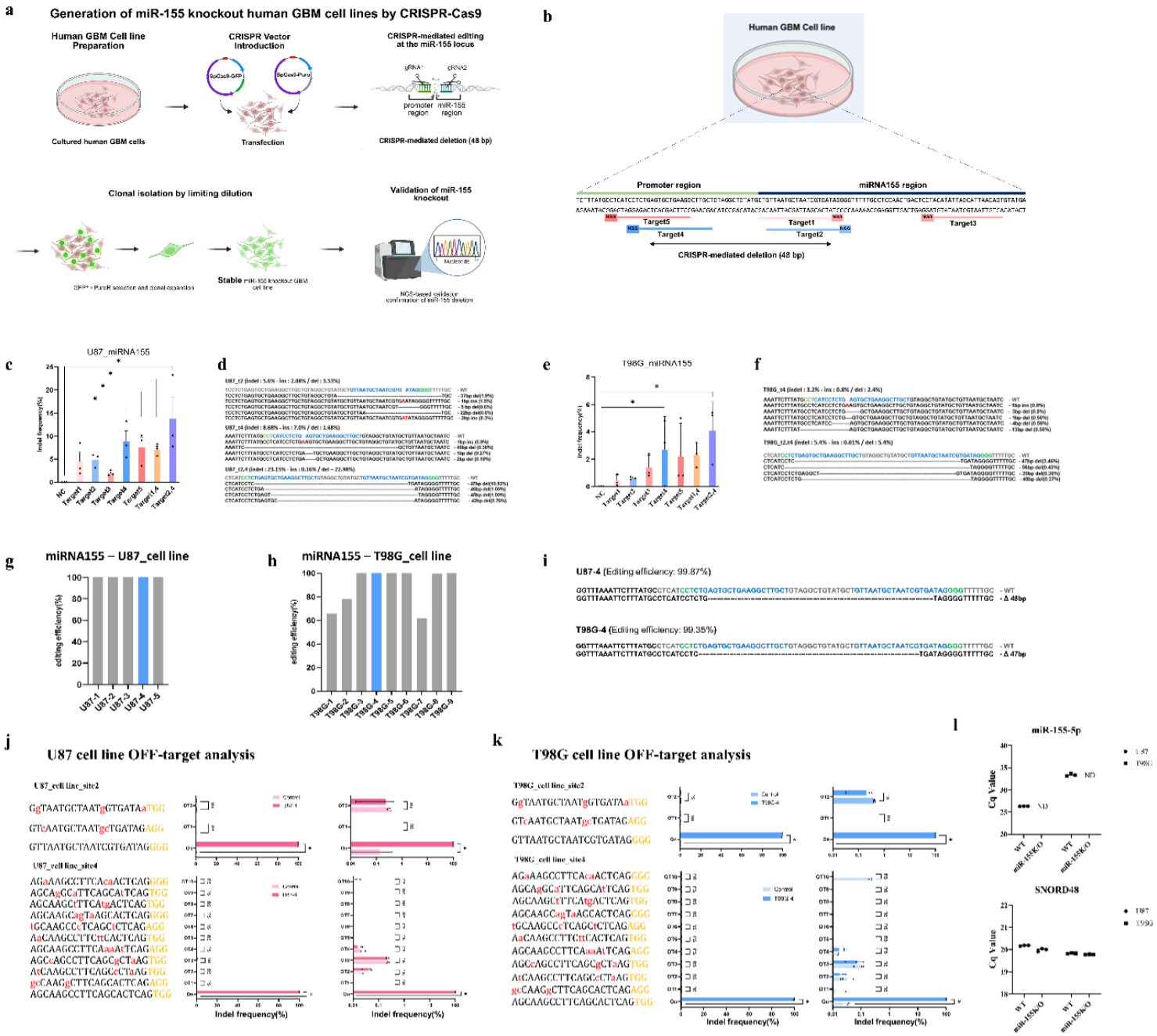


Figure 1

Generation and validation of CRISPR/Cas9-mediated miR-155 knockout GBM cell lines

(a) Experimental workflow for generating stable miR-155 knockout (K/O) U87 and T98G cells. Cells were co-transfected with SpCas9-GFP and SpCas9-Puro vectors carrying sgRNAs targeting the miR-155 locus, enriched by GFP fluorescence and puromycin selection, isolated by limiting dilution, and validated by targeted next-generation sequencing (NGS). **(b)**CRISPR/Cas9 targeting strategy for miR-155 deletion. Five sgRNAs were designed across the promoter and miR-155 regions; PAM sequences are indicated in red. **(c, e)** Indel frequencies induced by individual or paired sgRNAs in U87 **(c)**and T98G **(e)** cells, quantified by targeted deep sequencing. **(d, f)** Representative indel patterns at the miR-155 target locus

in edited U87 **(d)** and T98G **(f)** cells. Insertions are highlighted in red, and deletions are indicated by dashed lines. **(g, h)** Editing efficiencies of single-cell-derived U87 **(g)** and T98G **(h)** clones. **(i)** Sequence alignments of selected U87-4 and T98G-4 K/O clones, showing predominant 48-bp and 47-bp deletions with 99.87% and 99.35% editing efficiency, respectively. Target sequences are highlighted in blue, and PAM sequences in green. **(j, k)** Targeted deep-sequencing analysis of predicted off-target sites in U87-4 **(j)** and T98G-4 **(k)** cells. Mismatched bases are shown in red, with corresponding indel frequencies. **(l)** qRT-PCR validation of mature miR-155-5p expression. miR-155-5p was detected in wild type (WT) U87 and T98G cells but was not detected in miR-155 K/O clones under the assay conditions. SNORD48 Cq values are shown as endogenous reference-gene detection controls. ND, not detected. Data are presented as mean ± SEM. Statistical significance was determined by multiple unpaired t-tests with Holm–Šídák correction. ns, not significant; *P < 0.05, **P < 0.01.

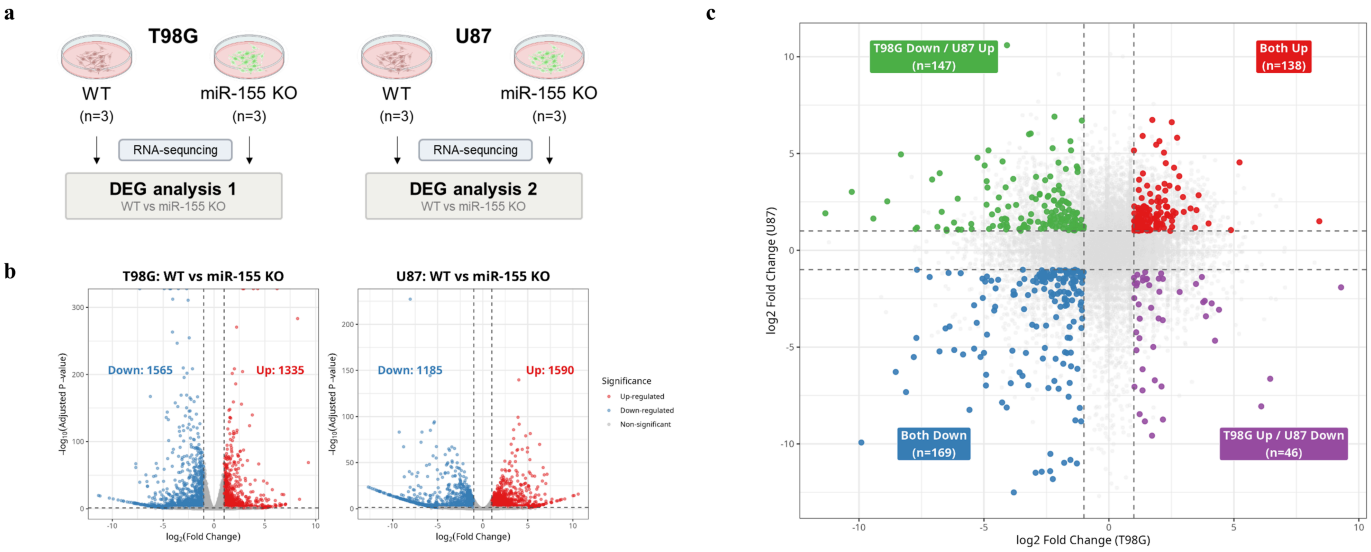


Figure 2

Transcriptome analysis design and overall transcriptomic changes

(a) Schematic diagram of transcriptome analysis in this study. **(b)** Volcano plots of DEG analysis 1 and 2. Blue dots indicate downregulated genes, red dots indicate upregulated genes, and black dots indicate non-significant genes with filtering criteria (padj < 0.05, $|\log_2 FC| \geq 1$). **(c)** Quadrant plot of DEGs in common in T98G and U87 cells. Log_2 fold change (LFC) values for T98G (x-axis) and U87 (y-axis) were plotted to compare transcriptome responses after miR-155 K/O. Significant differentially expressed genes were defined using the same threshold values as above. Gray dots indicate non-significant (NS) genes that did not meet statistical or fold change thresholds.

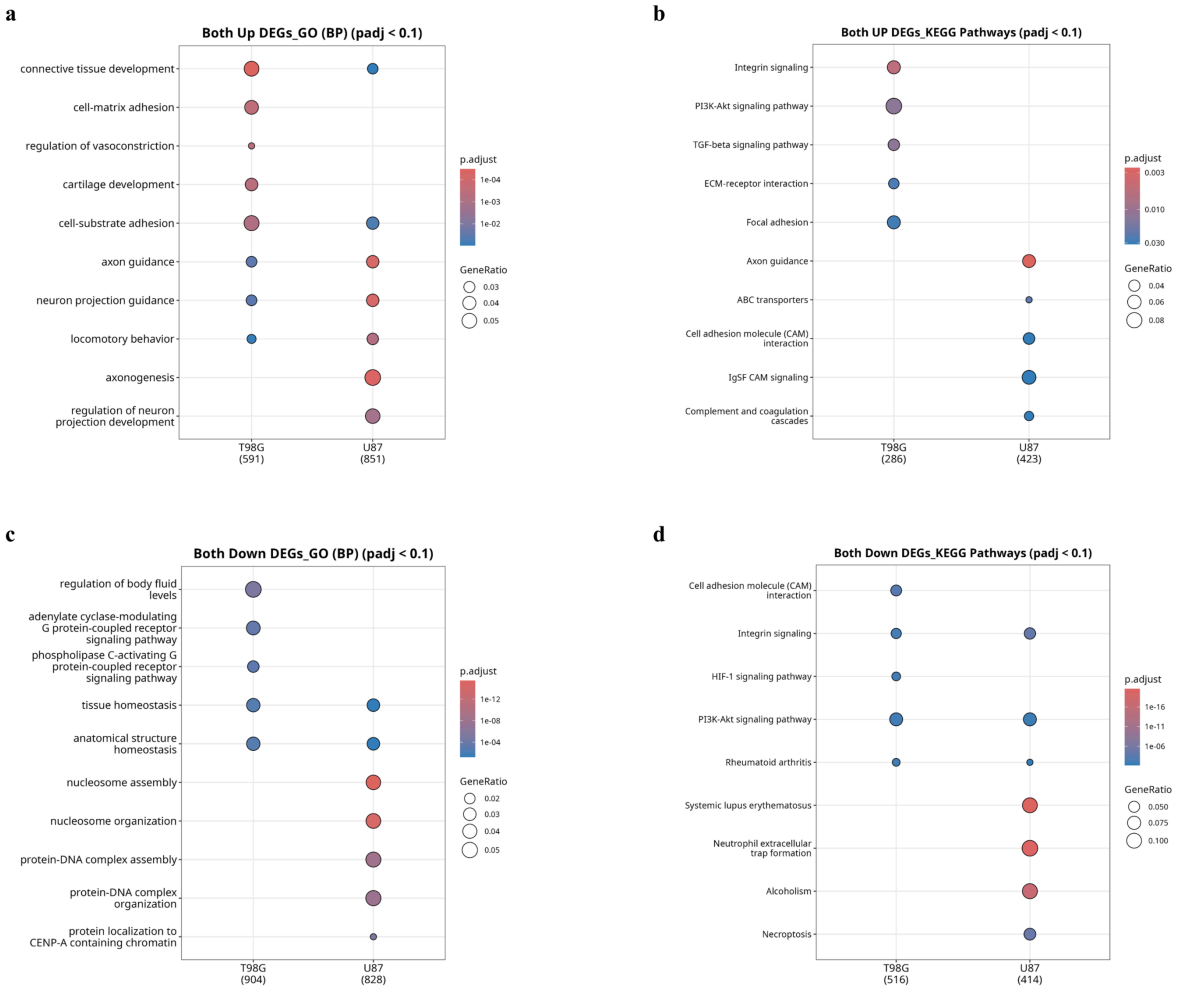


Figure 3

Comparative GO and KEGG enrichment analysis of DEGs in miR-155 K/O T98G and U87 cell lines

In the dot plot, the size of the dots is based on the proportion of genes associated with the corresponding GO term or pathway, and the color of the dots indicates the significance of the abundance. Numbers below the cell line names indicate the number of enriched genes. **(a)** Dot plot shows the up-regulated GO terms (padj <0.1) of biological process (BP) in both cells. **(b)** Dot plot shows the up-regulated KEGG pathways (padj <0.1) in both cells. **(c)** Dot plot shows the down-regulated GO terms (padj <0.1) of biological process (BP) in both cells. **(d)** Dot plot shows the down-regulated KEGG pathways (padj <0.1) in both cells.

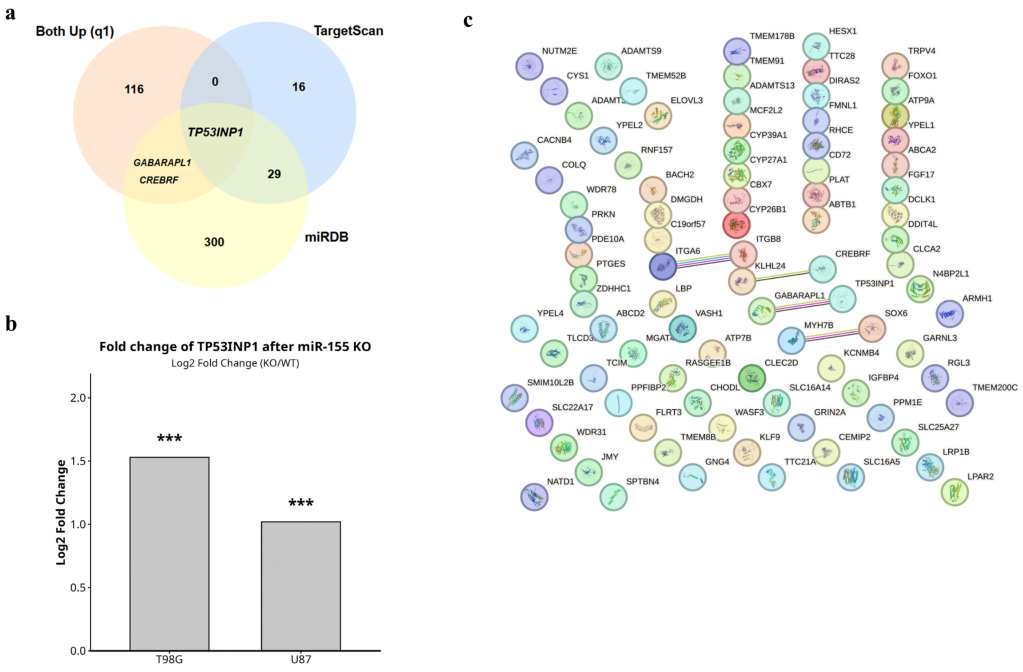


Figure 4

Prioritization and network analysis of candidate miR-155 targets

(a) Venn diagram comparing three miR-155 target gene datasets. The Both Up DEGs (q1) set became a final dataset of 120 genes through annotation and duplicate removal. **(b)** Bar graph showing TP53INP1 LFC values in miR-155 K/O U87 and T98G cells relative to their respective WT controls. ***P < 0.001. **(c)** Protein-protein interaction (PPI) network analysis of genes commonly upregulated in both miR-155 K/O GBM cell lines.

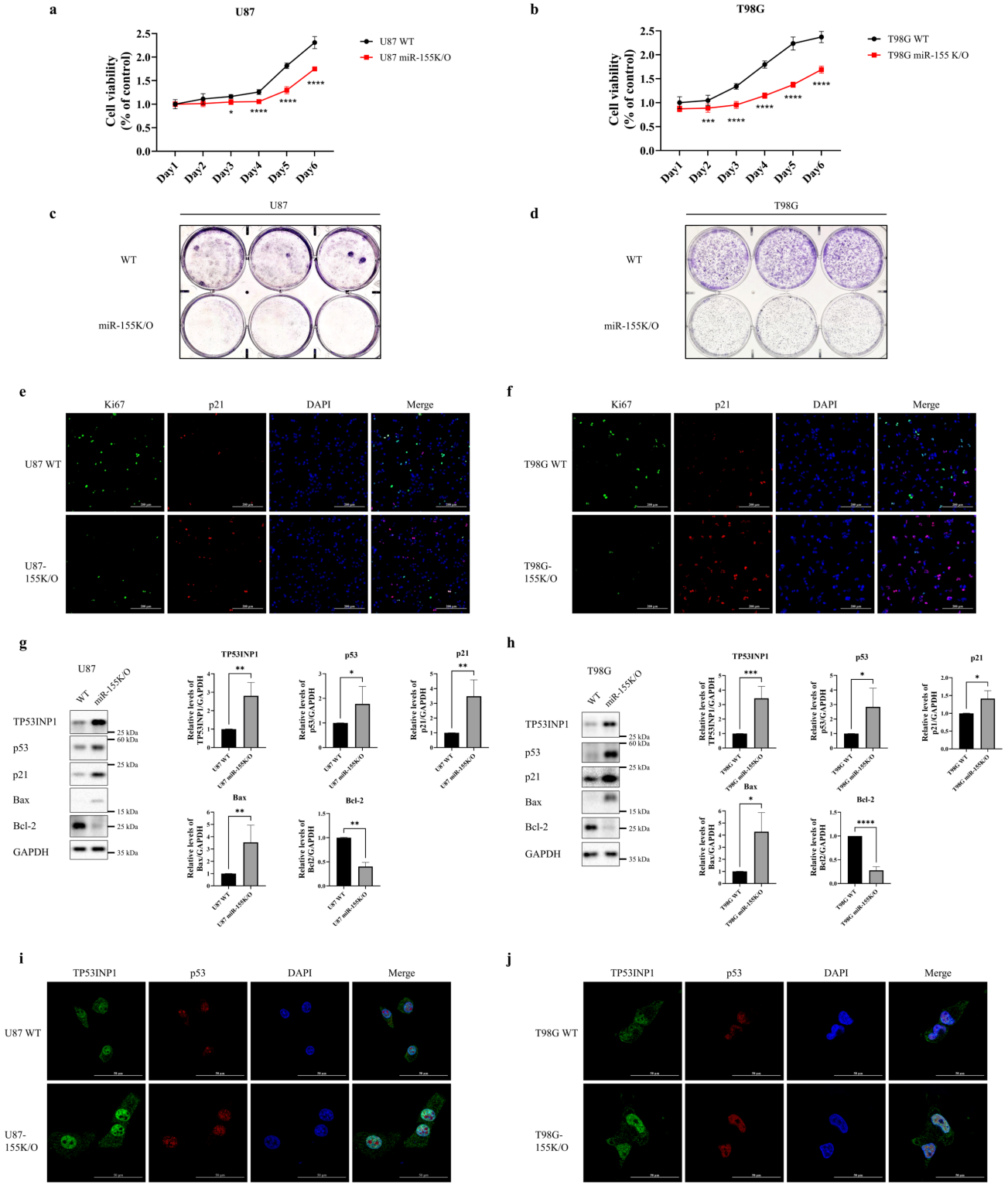


Figure 5

Stable miR-155 loss reduces proliferative activity and shifts TP53INP1/p53/p21-associated signaling in GBM cells

(a, b) Cell viability was assessed by MTT assay in WT and miR-155 K/O U87 **(a)** and T98G **(b)** cells. **(c, d)** Clonogenic assays were performed in WT and miR-155 K/O U87 **(c)** and T98G **(d)** cells. **(e, f)** Ki-67

(green) and p21 (red) immunofluorescence was analyzed by confocal microscopy in WT and miR-155 K/O U87 **(e)** and T98G **(f)** cells; nuclei were counterstained with DAPI (blue). **(g, h)** TP53INP1, p53, p21, Bcl-2 and Bax protein expression was analyzed by western blotting in WT and miR-155 K/O U87 **(g)** and T98G **(h)** cells. **(i, j)** Subcellular localization of TP53INP1 (green) and p53 (red) was examined by confocal microscopy in WT and miR-155 K/O U87 **(i)** and T98G **(j)** cells; nuclei were counterstained with DAPI (blue). Scale bars, 50 μm. Data are presented as mean ± SEM from independent experiments. Statistical significance for MTT assays was determined by two-way ANOVA followed by Šídák's multiple comparisons test. Statistical significance for other two-group comparisons was determined by two-tailed Welch's t-test. *P < 0.05, **P < 0.01, ***P < 0.001, ****P < 0.0001 vs WT.

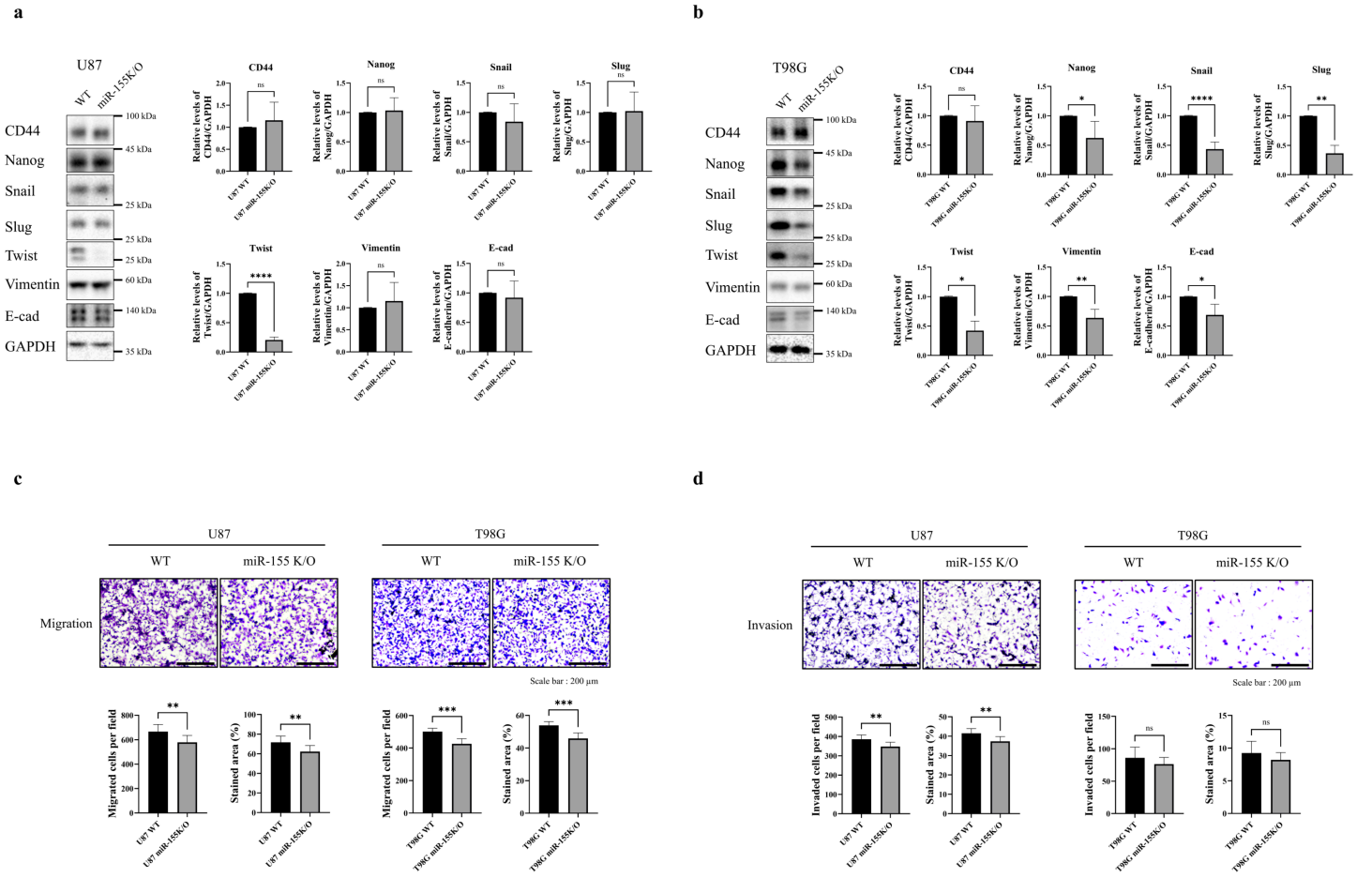


Figure 6

Heterogeneous effects of miR-155 K/O on EMT/stemness-related proteins and Transwell motility in GBM cells

(a, b) CD44, Nanog, Snail, Slug, Twist, vimentin, and E-cadherin protein expression was analyzed by western blotting in WT and miR-155 K/O U87 **(a)** and T98G **(b)** cells. **(c)** Cell migration was assessed by Transwell assay in WT and miR-155 K/O U87 and T98G cells. Representative crystal violet-stained images and quantification of migrated cell counts and stained area are shown. **(d)** Cell invasion was

assessed using Matrigel-coated Transwell inserts in WT and miR-155 K/O U87 and T98G cells. Representative images and quantification of invaded cell counts and stained area are shown. Scale bars, 200 μm. Data are presented as mean ± SEM from independent experiments. Statistical significance was determined by Welch's t-test. *P < 0.05, **P < 0.01, ***P < 0.001, ****P < 0.0001 vs WT; ns, not significant.

Supplementary Files

This is a list of supplementary files associated with this preprint. Click to download.

- supplementalinformation.zip